Thermodynamic determination of condensation behavior for the precursory elements of radioxenon following an underground nuclear explosion

Bernard Bourdon, Eric Pili

Thermodynamic determination of condensation behavior for the precursory elements of radioxenon following an underground nuclear explosion

Bernard Bourdon[1], Eric Pili[2]

[1]Laboratoire de Géologie de Lyon (LGL-TPE), ENS Lyon, CNRS and Université Claude Bernard de Lyon, 46 allée d'Italie, 69364 Lyon Cedex 7, France.

[2]CEA, DAM, DIF, F-91297 Arpajon, France.

Keywords: underground nuclear explosion, vaporization, condensation, indium, tin, antimony, tellurium, iodine, xenon

Abstract:

The measurement of radioactive xenon isotopes (radioxenon) in the atmosphere is a tool used to detect underground nuclear explosions, provided that some radioxenon escaped containment and that fractionation leading to the alteration of the relative proportions of these isotopes, is accounted for. After the explosion, volatilization followed by melting of the surrounding rocks produces a magma where the more refractory radioactive species get dissolved while the more volatile ones contribute to the gas phase that might escape. Indium, tin, antimony, tellurium and iodine are the main fission products involved in the decay chains leading to radioxenon. In this study, condensation as a function of temperature for these precursors of radioxenon were determined using thermodynamic calculations for systems with complex chemical composition corresponding to major environments of known underground nuclear explosions and for a range of pressure values representative of the cavity evolution. Our results illustrate a large difference between the relevant condensation temperatures for the radioxenon precursors and the tabulated boiling temperatures of the pure compounds often used as indicators of their volatility. For some precursory elements such as tin, the often-considered Heaviside function represents an oversimplification of the concept of condensation temperature, as condensation occurs over a temperature range as large as 2000 K. This results from the speciation of the elements in the gas phase mainly driven by the formation of oxides. Condensation also strongly depends on pressure while it moderately depends on the bulk chemical composition of the system. This study shows the

importance and complexity of the condensation process following underground nuclear explosions. It also shows how thermodynamic computations allow the prediction of the quantity and the relative proportions of radioactive xenon isotopes in the gas phase in the presence of magma, before their potential emission to the atmosphere. Better detection, discrimination and understanding of underground nuclear explosions should arise by taking into account the fractionation resulting from the condensation of the radionuclides producing radioxenon in nuclear cavities.

1. Introduction

The atmospheric detection of four radioactive isotopes (131m, 133m, 133 and 135 where m is for metastable) of xenon (Xe), altogether referred as radioxenon, possibly released at the ground surface following an underground nuclear explosion is a means for the verification of the Comprehensive nuclear Test Ban Treaty – CTBT – (UNODA, 1995; Carrigan et al., 1996; Hourdin and Issartel, 2000). Owing to many complex phenomena that occur after the explosion, it is difficult to relate the activity and relative proportions of the xenon isotopes detected in the atmosphere with the radioxenon inventory initially present in the nuclear cavity at depth. However, this is important to fully characterize the event. This difficulty pertains to the complexity of decay chains following fission together with a rapid thermal evolution and subsequent multiphase transport in geological media following the explosion (e.g., Sun et al., 2014, Sun and Carrigan, 2016; Pazdniakou et al., 2022) as well as the existence of an atmospheric background radioxenon signal not derived from underground nuclear explosions (Achim et al., 2016). One overlooked process that controls the availability of radioxenon is the partitioning of its precursory elements between the melt and gas phases in the nuclear cavity immediately after the explosion (Carrigan et al., 2020, Sun et al., 2021, 2022).

An underground nuclear explosion vaporizes the materials surrounding the detonation point and further melts the adjacent rocks (Taylor 1973). Upon cooling, condensation of the vaporized matter and melting of the cavity walls and debris leads to the production of a liquid whose composition depends on the surrounding rocks, while the material added by the nuclear device is comparatively small. As a result of nuclear fission, radioxenon is produced by three independent decay chains (e.g., Plompen et al., 2020). In the 131, 133 and 135 decay

chains (Figure 1), the main precursory elements for radioxenon are, successively, indium (In), tin (Sn), antimony (Sb), tellurium (Te), iodine (I), which are all more refractory elements than xenon (Xe). Therefore, depending on the cooling history of the nuclear cavity together with the short-lived existence of the nuclides controlled by the decay chains, the precursory elements may condense into the magma or on the colder surfaces of rocks (cavity walls or chimney rubbles) before radioxenon may have escaped the nuclear cavity and started percolation through the fractured geological media towards the atmosphere. If condensation is sufficiently rapid compared to decay, the production of the various radioxenon isotopes in the vapor phase of a nuclear cavity can be altered.

Thus, in order to make more accurate predictions about the composition of the Xe isotopes possibly emitted to the atmosphere, it is necessary to know whether the precursory elements will condense before radioxenon escapes the system. As such, the condensation temperatures and vapor pressures of the elements give quantitative information on their existence in the gas phase. In this study, we have determined the equilibrium conditions of the vapor-magma system from which we deduced condensation temperatures and vapor pressures for the chemical composition of silicate liquids produced by melting of basaltic or granodioritic rocks after an underground nuclear explosion.

2. Phenomenology of underground nuclear explosion and how it relates to our calculations

Following a nuclear explosion, the energy is released within a timescale of microseconds and propagates as a shock wave from the detonation point. In the region where enough shock energy is deposited, about 70 tons (per kiloton (kT) of explosive energy) of material reaches temperatures large enough to complete vaporization (Butkovich 1974a). Beyond this zone of full vaporization, the deposited energy is sufficient to fully melt in the order of 1000 tons of material (per kT of explosive energy), depending on the initial density of the rock (Butkovich 1974b). The vapor that is produced by the explosion expands and forms a cavity containing both melt and vapor. The volume of the cavity is controlled by the depth of the explosion, the energy released and the local rock nature, the density and the water content (Boardman et al., 1964; Higgins and Butkovich, 1967; Higgins, 1970; Butkovich, 1974b). In our study, we have focused on the initial system consisting of vapor and magma evolving with decreasing pressure and temperature as the initial energy is dissipated in the geological medium. This corresponds to an early stage depicted in Figure 7 of Schwartz et al. (1984) where the magma

exists together with a vapor phase in a spherical cavity (from ca. 500 msec) until the collapse of the cavity roof into the magma puddle (a few seconds to a few hours later). This potentially gives enough time for thermal and chemical equilibrium to take place between the magma and the gas phases, relative to the timescales of the radioxenon decay chains considered here. The system cools relatively rapidly and ultimately forms magmatic glass commonly analyzed for its radioactive content. Most of the budget of refractory fission products is observed to be contained in the magma (Borg 1975; Smith et al. 1996; 2003) rather than with the rubble that piles up at a distance from the magma found at the bottom of the cavity. This is a strong indication that the refractory elements that must have been initially vaporized upon the explosion were mostly condensed in the magma, rather than being dispersed in the surrounding geological medium. In contrast, there is evidence for a significant budget of more volatile elements that could have been partly transported to some extent by a vapor phase in the rubble pile, notably Sb (Smith et al. 1996; 2003) even if most of it is also contained in the magma. Thus, it seems reasonable to assume that at least in the beginning, there is a thermal and chemical equilibrium between the vapor phase and the magma as assumed in what follows.

3. Volatility of the elements and condensation temperatures

Chemical elements are considered as volatile if they preferentially partition in the vapor phase relative to condensed phases. One measure of this volatility is the condensation temperature. However, the condensation temperature of an element is not a fixed thermodynamic quantity since it depends directly on the ambient pressure. For a pure substance, in the case of a liquid-vapor equilibrium, the condensation temperature is only defined at a given pressure and corresponds to a point of the liquid-vapor curve in a P-T phase diagram. In this case, the saturation vapor pressure at equilibrium is defined by the Clausius-Clapeyron law, which is expressed for a vapor-liquid phase change. In the case of multi-component systems, such as the one studied here, at a given pressure, there is a range of temperatures for which the element considered will coexist in vapor phase and in liquid phase. The condensation curve is the curve representing the condensed fraction of the element as a function of temperature at a given pressure. In this context, it is common to define the condensation temperature as the temperature corresponding to an equal partitioning (50%, expressed in number of moles) between the condensed phase and the vapor phase.

Cosmochemists have defined condensation temperatures for a system with the chemical composition of the Sun at a pressure of 10^{-4} atm for all the elements of the periodic table (Lodders, 2003; Wood et al. 2019), this pressure corresponding roughly to that of the solar nebula in the vicinity of the Earth. Although these conditions do not correspond at all to that of nuclear explosions, it is informative to consider the condensation temperatures of the elements under these conditions (see Table 1). For pure substances, the boiling temperature is equal to the condensation temperature. For mixtures, the boiling temperature is composition-dependent and boiling will take place over a range of temperatures. The large difference between the condensation temperature and the boiling temperatures of the elements (Table 1) given at 1 atm comes largely from the pressure which is 10^{-4} atm. Another important parameter as will be discussed in detail is the bulk chemical composition of the studied system and the elemental speciation. By definition, the solubility of a volatile element in a silicate melt corresponds to the equilibrium concentration of this element in the melt at a given pressure. The condensation of an element in the silicate melt thus reflects its increasing solubility as the temperature is lowered, at a given pressure.

Table 1 Condensation temperatures determined for cosmochemistry and boiling temperatures

Element	Condensation temperature (K, at 10^{-4} atm)		Boiling temperature (K, at 1 atm)
	Lodders (2003)	Wood et al. (2019)	Lide (1990) and reference therein
In	492	536	2350
Sn	604	704	2876
Sb	890	979	1860
Te	665	709	1261
I	535	390	457

4. Oxygen fugacity, redox reactions and speciation

Depending on the condensation reaction describing the equilibrium between the vapor and liquid phase, the effect of oxygen fugacity can play a key role on volatility. This was for example demonstrated in the study of Ebel and Grossman (2000) who simulated conditions where the mass fraction of solid (mostly oxides) increased relative to H_2-dominant gas, which was

equivalent to increasing the oxygen fugacity. One observes that the condensation temperatures of elements are highly dependent on this O_2 fugacity but this earlier work did not include the trace elements (In, Sn, Sb, Te and I) that are the focus of the present study.

The experimental studies of Norris et al. (2017) and Sossi et al. (2019) have further illustrated the dependence of oxygen fugacity for trace elements but could not determine the corresponding condensation temperatures and vapor pressures for these elements due to non-equilibrium conditions of their experiments. For most trace elements dissolved in an oxide melt, the condensation temperature increases with oxygen fugacity (f_{O_2}). This can be understood if one writes the vaporization reaction of a metallic oxide (MO_{melt}), as:

$$MO_{melt} \leftrightarrows M_{gas} + \frac{1}{2}O_2 \quad \text{(R1)}$$

where M_{gas} is the vaporized metal species. If f_{O_2} increases, the reaction is favored towards the condensed phase (i.e. MO_{melt}), which is equivalent to increasing the condensation temperature. Thus, one needs to assess the redox state of the system and the speciation of the considered elements in the melt and in the vapor, to determine their volatility as a function of oxygen fugacity. These features as well as the dependence on the bulk composition of the system will be presented in what follows.

5. Thermodynamical approach

4.1. Initial conditions of the system and setup of the thermodynamic calculations

The trace elements (In, Sn, Sb, Te and I) which are the focus of this study are generated as fission products from the nuclear explosive and they initially partition in the vapor phase formed from the volatilization of the surrounding rocks.

The studies of Brode (1964), Egorov et al. (1979) and Taylor (1973) were used to set the post-explosion pressure and temperature conditions. The temperature and pressure conditions are in a transient regime with variable time constants which depend on the energy initially released during the explosion and later dissipated in the geological medium. The range in pressure (orders of magnitude of hundreds of bar to 1 bar, considered from the moment the chimney is formed) and temperature was chosen to cover the typical range reported in the literature on these topics (e.g. Chapin 1970; Butkovich 1974a). Model curves depending on the initial energy give the joint variation of T and P as a function of time (e.g., Egorov et al. 1979). These curves were used to establish the domains that needed to be explored from a

thermodynamic viewpoint. In this context, the pressure range used in this study was 1-100 bars (Taylor 1973; Egorov et al. 1979) and the temperature ranged between 500 and 4500 K. An additional feature that one should bear in mind is that the volatility of elements will not only depend on the thermodynamics but also on the kinetics, both of evaporation and condensation, and we assumed for the sake of simplicity that chemical equilibrium was reached. Some of these aspects are discussed below in section 8.1. By lowering the temperature at a given pressure, the elements are progressively condensed in the liquid phase starting with the most refractory to the most volatile.

As the relevant thermodynamic data were not available for temperatures greater than 2500 K, the thermodynamic parameters were extrapolated assuming that the parameterization obtained in Table 4 is valid for the 500-4500 K range of temperature.

In order to test the potential effect of the bulk chemical composition of the system on volatility, the condensation curves were calculated for two bulk silicate compositions reported in Table 2, a granodiorite and a basalt. These chemical compositions are of interest because they correspond to two extreme compositions typical of terrestrial rocks likely to be observed at underground nuclear test sites. Granodiorites and basalts both occur at the Nevada National Security Site (Sinnock 1982) or the Cannikin Site, Alaska (Lee and Gard 1971). Basalts occur in most oceanic islands, particularly in atolls, such as the former French nuclear test sites at Mururoa and Fangataufa (IAEA, 1998b). Granodiorite is also a close approximation of the chemical composition of rocks from the Semipalatinsk (formerly USSR, now Kazakhstan) nuclear test site (IAEA, 1998a) and of the North Korean nuclear test site at Punggye-ri (Coblentz and Pabian, 2015). The composition of the granodiorite considered is a typical composition taken from the GERM database (earthref.org/GERM). The composition of the Mururoa basalt is taken from Dupuy et al. (1994). The In, Sn, Sb, Te and I contents are fixed arbitrarily at 10^{-6} mol/100 g (*i.e.* in the range 0.11-0.13 ppm) such that they can be considered as trace elements. This content is 1 to 2 orders of magnitude larger than the nuclear fission contribution to each of these elements, considering conservatively 10^{-2} mol of each isotope for a 1 kT explosion and 400 kg of melt (Sun et al., 2014; Carrigan et al., 2020). Hence, the elemental concentrations considered here also account for the natural contents of rocks in In, Sn, Sb, Te and I. The exact values selected here have no influence on the calculated condensation temperatures, as long as the elements are at the trace level.

Table 2: Chemical compositions of silicate rocks representing the bulk composition of the system.

Oxides	Granodiorite[1] wt %	Basalt[2] wt %
SiO_2	57.41	46.15
Al_2O_3	16.7	16.53
TiO_2	1.52	3.75
Fe_2O_3	8.58	11.55
MnO	0.16	0.11
MgO	3.14	4.27
CaO	4.86	9.68
Na_2O	3.8	3.71
K_2O	3.04	1.41
P_2O_5	0.29	0.45
H_2O	1.0	1.96

[1]From GERM database, [2]from Dupuyet al. (1994).

4.2. Thermodynamic database and calculations

The chemical equilibrium at various temperatures and pressures was calculated using the FactSage™ software (Bale et al. 2016), which includes thermodynamic databases for major elements as well as for many trace elements. The FToxid (oxide solutions) and FTpure (pure compounds) databases were used in this study. The Ftoxid database includes specific thermodynamic models for solutions of molten oxides (SLAG-A and SLAG-F). It is possible to manually add thermodynamic data, such as activity coefficients that are not part of the database, especially for dealing with trace element levels. We used this feature to include the trace elements In, Sn, Sb and Te. For the case of iodine, we used a specific molten oxide solution that includes I in the FactSage™ database (SLAG-F) which is distinct from the more complete oxide model used for the other elements (SLAG-A).

The FactSage™ software calculates thermodynamic equilibrium using minimization of the Gibbs energy of the total system. The total Gibbs energy of the system can be written as:

$$G_{tot} = \sum_j \sum_i \mu_i^j n_i^j \qquad (1)$$

Where i represents a given constituent in a phase j and μ_i is the chemical potential of constituent i in phase j, n_i is the number of moles of constituent i. This equation can be further expanded to show the importance of activities and fugacities:

$$G_{tot} = \sum_j \left(\sum_k \left(\mu^j_{k\,0} + RTlnf_k \right) n^j_k + \sum_l \left(\mu^j_{l\,0} + RTlna_l \right) n^j_l \right) \qquad (2)$$

where index k and i are for the vapor phase and condensed phases, respectively, and f_k and a_l are the fugacity and activity of component k and il respectively, in phase j. This approach requires a knowledge of all the thermodynamic properties of all the species contained in the vapor (i.e. their fugacities) and of the mixing properties of the liquid phase and of the solid phases that form solid solutions. Using the activities of all constituents, it is possible to calculate the partial Gibbs energy of each constituents (i.e. their chemical potential) and then optimize the phase proportions to minimize the total Gibbs energy of the system. These calculations assume that the whole system (with a bulk composition specified in Table 2 for the vapor+magma phases considered together) reaches chemical equilibrium at constant temperature and pressure, which is an important assumption whose validity is discussed in Section 8.2.

For a given T and P, the composition and abundance of each stable phase is calculated. The calculation also yields the speciation in the vapor phase. Our calculations were done at fixed pressures of 1, 10, 50 and 100 bars for temperatures ranging between 4500 and 500 K with temperature steps of 100 K.

The volatility of elements depends on their activity in the solid or liquid phase. For the vaporization reaction (R1), the equilibrium constant can be written as:

$$K_{P,T} = \frac{f_M {f_{O_2}}^{1/2}}{a_{MO}} = \frac{f_M {f_{O_2}}^{1/2}}{\gamma_{MO} X_{MO}} \qquad (3)$$

where f_i represents the fugacity of component i and a_{MO} is the activity of MO in the silicate melt, γ_{MO} its activity coefficient and X_{MO} its molar fraction. This equation shows that the volatility depends directly on the oxygen fugacity, a parameter controlled by the major element composition, rather than the trace element itself. While the vapor pressure will depend on the concentration of M in the source material, the calculated condensation temperature will be independent of this parameter because it is calculated by the ratio of molar abundances (see caption of Figure 3). This equation also shows that volatility expressed by the fugacity of vapor species M(g) depends on the activity coefficient in the oxide solutions.

This parameter depends itself on the chemical composition of the system and on the interaction parameters of element M with other constituents. We calculated volatility of In, Sn, Sb, Te and I using literature data for the activity coefficients as reported in Table 3 following the methodology described in the next section.

6. Determination of activity coefficients

The activity coefficients of In, Sn, Sb and Te have been measured experimentally for silicate melts of various compositions but these data are not included in the FactSage™ databases. In contrast, the FactSage™ SLAG-F database already includes activity coefficients for iodine in silicate melts in dilute concentrations.

6.1. Existing activity coefficients for iodine, indium, antimony and tellurium

For iodine, it has been shown that the most of it is in the form of I^- (McKeown et al. Muller et al. 2014; Cicconi et al 2020) and that iodide is often associated with alkalis (Na and K essentially) or with calcium, which is consistent with the components present in the SLAG-F solution of FactSage™. Previous experimental studies (Musselwhite et al. 2000; Cicconi et al. 2019; Riley et al. 2014; Jolivet et al. 2020) focusing on iodine solubility have not determined directly the iodine activity in silicate melts and this would deserve dedicated experimental studies in the future.

For indium, experimental determinations of activity coefficients reported in the study of Norris (2016) give a mean value of 0.030 with a range from 0.0025 to 0.12 at a temperature of 1923 K. For Sb, there are several determinations of the activity coefficient of $SbO_{1.5}$ in oxide mixtures, including those given in Norris (2016). Mendoza et al. (2001) have determined the activity coefficient for $SbO_{1.5}$ in CaO-FeO-SiO_2 mixtures as a function of the CaO content in oxide melts and show variations of this parameter between 1.8 and 3.9 at 1573 K. These values are rather close to the range in activity coefficients given in Norris (2016) at 1923 K (0.11-8.9, mean=2.3). Thus, we have used values from the experiments of Norris (2016) and the results are given in Table 4. A Raoult activity coefficient of $SbO_{1.5}$ equal to 1.14 at 1923 K was reported by Tan et al. (2001). However, a Raoult activity coefficient corresponds to that of a solvent and is equal to 1 for a molar fraction of $SbO_{1.5}$ equal to 1. This is not the same reference state as that used for trace element where Sb is expected to be at infinite dilution (Henry activity coefficient).

Johnston et al. (2010) reported values of the activity coefficients of Te in silicate melts (SiO_2-CaO-FeO) and showed a weak dependence on temperature and on CaO contents.

6.2. The case of tin: SnO versus SnO_2

Shuva et al. (2016) compiled the activity coefficients of SnO-SnO_2 in silicate mixtures, with values ranging between 0.8 and 6 (Rankin et al. 1986, Takeda et al. 1990; Nagamori and Mackey 1978). However, these values are relevant for SnO rather than for SnO_2 as these data were obtained at low oxygen fugacities, where SnO is the only stable species in the silicate melt. By comparison, the values of the activity coefficient for SnO_2 given in Norris (2016) for experiments in graphite capsules were orders of magnitude smaller (3×10^{-3} to 9×10^{-5}). The same parameter was also estimated by Gortais et al. (1994) at a temperature of 1500 K but the oxygen fugacity was not given, yielding γ_{SnO2} values between 0.2 and 2.5.

As this parameter can greatly affect the volatility of this element, in what follows, we first checked that the oxygen fugacity in the conditions of an underground nuclear explosion leads to the SnO_2 species, not SnO, to be dominant in the silicate melts. It is possible to extract the SnO_2 activity coefficients from reported experiments that were initially designed to determine the metal-silicate partition coefficient for Sn (Wood et al., 2013). These metal-silicate experiments involve the following exchange reaction for tin:

$$SnO_2^{sil} \leftrightarrows Sn^{met} + O_2^{gas} \quad \text{(R3)}$$

Combining with the reverse reaction for iron that represents the major element in the considered experiments, the reaction can be rewritten:

$$2Fe^{met} + SnO_2^{sil} \leftrightarrows Sn^{met} + 2FeO^{sil} \quad \text{(R4)}$$

Its equilibrium constant can be expressed as:

$$K = \frac{a_{Sn}^{met} a_{FeO}^{sil\ 2}}{a_{SnO_2}^{sil} a_{Fe}^{met\ 2}} = \frac{X_{Sn}^{met} X_{FeO}^{sil\ 2}}{X_{SnO_2}^{met} X_{Fe}^{met\ 2}} . \frac{\gamma_{Sn}^{met} \gamma_{FeO}^{sil\ 2}}{\gamma_{SnO_2}^{sil} \gamma_{Fe}^{met\ 2}} \quad (4)$$

One can see that the equilibrium constant is a function of the parameter we are interested in (i.e. $\gamma_{SnO_2}^{sil}$). Thus, provided all the other parameters are known, one can express the activity coefficient of SnO_2 in the silicate melt as a function of the equilibrium constant K and the other parameters. First, this equilibrium constant can be calculated at the temperature of

interest using the free enthalpies of formation of the pure compounds Fe, FeO, SnO_2 and Sn reported in thermodynamic tables (Barin 1995). The free enthalpies of formation of each reagent and product are used to calculate the free enthalpy of the reaction R4:

$$\Delta^R G = G_f^{Sn} + 2G_f^{FeO} - G_f^{SnO} - 2G_f^{Fe} \qquad (5)$$

This equation is then converted to an equation giving the equilibrium constant of reaction R4:

$$LnK = \frac{-\Delta^R G}{RT} = 2LnK_f^{FeO} + LnK_f^{Sn} - \left(2LnK_f^{Fe} - LnK_f^{SnO_2}\right) \qquad (6)$$

The formation constants of SnO_2 and FeO can then be parameterized as a function of 1/T using the data of Barin (1995), with the formation constant of pure Sn and Fe being equal to zero, by definition. One obtains for SnO_2 (valid between 1300 and 1800 K):

$$Ln\ K_f^{SnO_2} = \frac{68377}{T} - 23.795 \qquad (7)$$

and for FeO (equation valid between 1650 and 2500 K):

$$Ln\ K_f^{FeO} = \frac{31217}{T} - 6.6503 \qquad (8)$$

Based on these equations, one can extract the activity coefficient of SnO_2 in the silicate melt:

$$Ln\ \gamma_{SnO_2}^{sil} = Ln\ \frac{X_{Sn}^{met} X_{FeO}^{sil}}{X_{SnO_2}^{met} X_{Fe}^{met}} . \frac{\gamma_{Sn}^{met} \gamma_{FeO}^{sil}}{\gamma_{Fe}^{met}} - 2LnK_f^{FeO} + LnK_f^{Sn} - \left(2LnK_f^{Fe} - LnK_f^{SnO_2}\right) \qquad (9)$$

The parameters X_{Sn}^{met}, X_{FeO}^{sil}, $X_{SnO_2,}^{met}$ X_{Fe}^{met} can be determined for each bulk composition of the silicate melt in the metal-silicate experiments (as given in Righter et al. (2017) in the case of Sn) while the activity coefficients of FeO in the silicate melt are known from the literature (e.g., Wood and Wade 2013). The activity coefficient of metallic Sn in molten iron alloys can be calculated using the interaction parameters between the constituents of alloys as described in Ma (2001). The values of the interaction parameters have been recently compiled by Righter et al. (2017) and are also given in a compilation by the Japan Society for the Promotion of Science (1988). Since all the parameters of equation (8) can be calculated independently for the chemical composition of each reported metal-silicate experiment, it is then possible to calculate individual values of the activity coefficient of SnO_2 in the silicate melts. Thus, based on equation (8), one can determine from the above equations the values of $\gamma_{SnO_2}^{sil}$ although this parameter has never been directly determined experimentally.

By using this methodology, we have calculated the activity coefficients for two series of experiments, one with a graphite capsule and one with an MgO capsule (Righter et al. 2017). The activity coefficients obtained in both cases differ by at least one order of magnitude.

However, one should note that the experiments involving graphite (implying a large concentration of C in the metal) yield γ_{SnO2} activity coefficients ranging between 10^{-2} and 10^{-4} which are comparable to those obtained by Norris (2016) with experiments involving also graphite. However, these experiments do not correspond to the situation found in underground nuclear explosions where the C level of the environment is rather low for the rock compositions studied here. We contend that an uncertainty on the interaction coefficient of C with Fe or Sn could produce differences in the γ_{SnO2} values. The experiments of Righter et al. (2017) with an MgO container yield values that are closer to those of Gortais et al. (1994) and we have used these values to calculate the volatility of Sn (see below). Based on these values of the activity coefficient for SnO_2, we obtained a regression line as a function of temperature (Figure 2). For a given chemical composition, temperature is the most important source of variation of the Sn activity coefficient.

6.3. Parameterization of activity coefficients: dependence on temperature and on the chemical composition of the system

We were able to obtain a set of activity coefficients, based on the above compilation of literature data for In, Sb and Te, and on the FactSage™ database for iodine, as well as on the calculation of Sn activity coefficient using the method described in Section 6.2. Some typical values are given in Table 3. One could note that these activity coefficients largely deviate from 1. Given their temperature dependence, it is important to use a parameterization rather than a constant value, whenever possible, as detailed in what follows.

In order to express their variations as a function of temperature the following equation was used:

$$Ln(\gamma_i) = \frac{A}{T} + B \qquad (10)$$

where A and B are constants that are determined experimentally.

Table 3 Speciation and source of activity data used in the calculations

Element	Species	Temperature of experimental determinations (K)	Source of activity data
In	$InO_{1.5}$	1873	Norris (2016)

Sn	SnO_2	1773-2173	Righter et al. (2017)
Sb	$SbO_{1.5}$	1873	Norris (2016)
Te	TeO	1573	Johnston et al. (2010)
I	I	N/A	FactSage™ (Slag F)*

382

383

384 **Table 4 Parameterization of activity coefficients as a function of temperature according**
385 **equation (9) for two chemical compositions of the system**

Composition	In	Sn	Sb	Te	I
Basalt	A = -22195	A = 7527.7	A=5050.28	A=1415.7	A=934.15
	B=0	B = 4.5393	B=0	B=0	B=4.8917
Granodiorite	A=-30055	A = 7527.7	A=-7025.68	A=1415.7	A=-1260.2
	B=0	B = 4.5393	B=0	B=0	B=0.8657

386

387

388 For In and Sb, twenty-four experiments reported in Norris (2016) were used to calculated the
389 parameterization of the activity coefficients as reported in Table 4. For tellurium and tin, there
390 is a more limited set of experiments (Johnston et al., 2010) or limited variations in the chemical
391 composition of the silicate (Righter et al. 2017) and thus no dependence on composition was
392 assumed as shown in Table 4.
393 A second step (if sufficient data is available) was to parameterize the variations in activity
394 coefficients as a function of the various chemical compositions for the systems studied here.
395 This was done by using the model proposed by O'Neill and Eggins (2002), which can be
396 described by the following equation valid for a given temperature:

397 $$ln\gamma_i = \sum_{j=1}^{n} \sum_{k=1}^{j} a_{ij} X_j X_k \qquad (11),$$

398 where i and j refer to the chemical components listed in Table 2. It is considered here that the
399 trace elements have little influence on each other in the silicate mixtures. This summation
400 implies cross-terms (X_jX_k) and quadratic terms such as X_j^2.

401

402 **7. Results of condensation temperature calculations**

403

7.1. Reference calculations without solubility or with ideal mixing

For the sake of comparison with more complete calculations (as detailed below), we first produced simplistic thermodynamic simulations. As an initial experiment, we consider no solubility of In, Sn, Sb, Te and I in the silicate melt. In this case, the condensation of these elements is implicitly controlled by the condensation of pure compounds, i.e. indium oxide (In_2O_3), cassiterite (SnO_2), cervantite (SbO), tellurite (Te_2O_3), and lautarite $Ca(IO_3)_2$ (this species is the first to be saturated among all other species present in the database). Their vapor pressures were calculated at a pressure of 50 bars for a basaltic composition and their condensation curves are shown in Figure 3. The condensation temperatures for In, Sn, Sb, Te and I are given in Table 5. Second, one can also assume that each of these elements can form an ideal mixture with the silicate melt assuming that the activity coefficients are equal to 1 (Henry activity coefficient for infinite dilution). The resulting condensation curves are depicted in Figure 4, also at a pressure of 50 bars for a basaltic composition. They are significantly offset compared with the previous calculations (Fig. 3). The condensation temperatures for In, Sn, Sb, Te and I are given in Table 5. These results show that assuming ideal dissolution in a silicate melt will produce higher condensation temperatures than for the case of pure substances. As we shall see below, since the solution is not ideal, these condensation temperatures have to be further refined.

7.2. Condensation in conditions relevant to underground nuclear explosion conditions

The activity coefficients determined with the methods presented above were used to calculate equilibrium vapor pressures and condensation temperatures relevant for the P-T conditions and bulk chemical composition of an underground nuclear cavity. The corresponding condensation temperatures are given in Table 5. The condensation curves calculated at four discrete pressures (1-10-50-100 bar) are shown in Figures 5 and 6 for the basalt and granodiorite compositions given in Table 2. The calculations were carried up to a temperature of 4500 K. For the pressures above 50-100 bars, the initial fraction in the vapor phase is in some cases slightly below one, indicating that the condensation has started at a temperature slightly higher than 4500 K. However, these high pressures and temperatures correspond only to a short transient state of the system, when there is little time for elemental fractionation due to the half-lives of the considered elements (Plompen et al., 2020). It should be mentioned here that the calculation of activity coefficients was not extrapolated beyond

4500 K, which means that the upper limit of the pressure in our calculations is approximately 100 bars. Iodine condenses at a much lower temperature than the other elements and it remains a volatile element until 500-600 K with only limited solubility in the silicate melt. Iodine finally condenses as lautarite ($Ca(IO_3)_2$), which suggests that there is only limited partitioning of I in the silicate or oxide minerals that are saturated at these temperatures such as feldspar, quartz, sphene or rutile (see also Musselwhite, 1995).

Figure 7 shows the variation of condensation temperatures with pressure for the granodiorite (Figure 7a) for the basalt (Figure 7b). As expected, there is a general increase in condensation temperature with pressure but this increase depends on the condensation reactions. In addition, the condensation of each element takes place over a wider range of temperatures than for a pure element. This can be interpreted as resulting from the presence of solutions (here a silicate liquid) as well as from the vapor speciation of each element that changes with temperature.

The condensation temperatures are distinct from the boiling temperature of pure compounds used in the study of Carrigan et al. (2020) and Sun et al. (2021) to describe condensation of the elements of interest. For example, at 1 bar, Sn is more volatile than In in a silicate melt, while it is the reverse for metallic indium and metallic tin (see Table 1 for the boiling temperature of the pure metals). Last, at the same pressure of 1 bar, the condensation temperature for a given element can be offset by a few to several hundreds of kelvins compared with the boiling temperature (for Sb, 2697 K (granodiorite) or 1640 K (basalt) instead of 1760 K for the boiling temperature of metallic antimony at 1 bar).

Table 5 Condensation temperatures (kelvin) calculated for In, Sn, Sb, Te and I in a nuclear cavity at 4 pressure values for two host rock compositions

Rock composition and pressure	In	Sn	Sb	Te	I
Granodiorite 1 bar	3407	2389	2697	1122	499
Granodiorite 10 bar	3869	2959	3107	1718	550
Granodiorite 50 bar	4101	3579	3475	1921	600
Granodiorite 100 bar	4159	3934	3645	2021	650

Basalt 1bar	3075	2250	1640	__	500
Basalt 10 bar	3445	2840	1800	__	550
Basalt 50 bar	3820	3526	2689	1940	600
Basalt 100 bar	3838	3930	2893	1970	649
Basalt 50 bar (pure substances)	2964	3637	2154	2144	578
Basalt 50 bar (ideal mixing)	1310	3627	1748	875	557

If one compares the condensation temperatures as a function of the chemical composition, one notices significant variations between the granodiorite and basaltic cases. For example, there is a 500 K offset for the Sb condensation temperature between the granodiorite and the basalt. This can be partly explained by the variation in activity coefficients that range between 0.38 (basalt at 2000 K) and 2.0 (granodiorite at 2000 K).

The activity coefficients used in this study were derived from experimental studies and extrapolated to the relevant temperatures or chemical compositions, when available. These calculations could be improved by experimental measurements of activities for a range of temperatures and for the actual chemical compositions of the magma found after underground nuclear explosions. These activity measurements could be made thanks to a Knudsen Effusion Mass Spectrometer, as illustrated in Costa et al. (2017) who studied the vaporization of olivine which is a common silicate mineral found in basalts and mantle rocks.

8. Potential caveats

8.1. Kinetic barriers to condensation: possible deviations from equilibrium calculations

The condensation of a vapor has been studied from a theoretical and experimental viewpoint by physical chemists. Thus, the main parameters that control the kinetics of condensation are known (e.g., Hirth and Pound 1963; Mutaftschiev 2001). First, the initial step for starting condensation is to start the nucleation of a droplet or a crystal and this requires that the system must overcome the so-called nucleation barrier which represents the minimum energy to nucleate. This energy barrier depends on the level of oversaturation, i.e. the pressure of the species that condensate relatively to the equilibrium pressure or vapor pressure. It is well known that the greater the overpressure, the smaller this energy barrier. Second, the nucleation is considerably eased up by the presence of a substrate. The substrate could consist of the host rock or of aerosols that may form in the vapor phase. In this case, the energy

barrier for nucleation can be lowered by a factor that depends on the wettability of the condensing liquid onto the substrate.

Independently of these considerations, the rate of condensation dn_i/dt onto a surface can be described by the Hertz-Knudsen equation that illustrates directly the dependence of condensation rates on the degree of oversaturation (Hirth and Pound 1963):

$$\frac{dn_i}{dt} = \frac{\gamma_i P_i}{\sqrt{2\pi m_i RT}}\left(1 - \frac{P_{i,sat}}{P_i}\right) \qquad (12)$$

γ_i is the condensation coefficient, P_i and $P_{i,sat}$ are the partial pressure and the saturation pressure of species i, m_i, its mass. This equation also shows the importance of a second parameter, which are the condensation coefficients. This parameter is directly linked with the probability for a vapor species to actually condensate once it hits a liquid or solid surface. As this parameter can be considerably lower than one, this means that the condensation rate can be significantly lower than what is predicted with the common assumption of a γ_i value equal to 1. In a comprehensive model of condensation from a vapor formed in a nuclear cavity, all these parameters would need to be taken into account.

8.2. Potential complications arising in the conditions of underground nuclear explosions

As stated above, our calculations were done for a closed system evolving in chemical equilibrium at fixed pressure with a fixed amount of volatile species such as water. Real systems could exhibit additional complexities, which could produce significant deviations compared with what was calculated here. These potential complications are briefly reviewed here based on existing literature.

In the initial stages following the explosion, the vapor in the cavity can reach temperatures that are higher than the country rock at the boundary of the cavity, as described in Chapin (1970). Our calculations therefore do not apply to this stage. However, as explained in Chapin (1970), there is a rapid cooling of the overheated vapor until thermal equilibration is reached. Another issue that is particularly relevant regarding the more volatile elements among those studied here is that the vapor could cool by radiative heat loss or adiabatic expansion into fractured rocks outside the cavity. In this case, the system that we study should not consist of magma + vapor, as one could consider that the vapor gets isolated from the magma. This decoupling could take place at pressures of 30-50 bars (Higgins and Butkovich, 1967). Another consideration that may play a role is that the diffusion timescale of the Xe precursors in the

519 magma might get slower as the temperature decreases. As shown in Figure 8a, for
520 temperatures below 3000-3500 K, the diffusion length scales of Te, Sb and Sn in a basaltic melt
521 decrease considerably, which argues against equilibration between vapor and magma in this
522 case. To further consider the effect of vapor isolation, we have calculated in the case of the
523 basaltic composition at 50 bars, the condensation temperatures of In, Sn, Sb and Te from an
524 isolated vapor produced at 3500 K. The results are plotted in Figure 8b and show that there
525 can be a significant shift in the condensation temperature corresponding to this situation. This
526 calculation illustrates that it is possible to take into account such a complication, provided a
527 reasonable scenario is considered.
528 The heating of the cavity walls can lead to the vaporization of water that can then mixed with
529 the existing vapor inside the cavity (e.g. Chapin 1970). In this case, the water content of the
530 initial vapor could exceed the bulk composition of the rock (i.e. basalt or granodiorite in our
531 cases). In order to consider the effect of this excess water on the condensation temperatures,
532 we have calculated the condensation temperature by increasing by a factor of 2 and a factor
533 of 10 the amount of water contained in the basaltic composition (Table 2). The results
534 obtained for the condensation temperature are shown in Figure 9. By increasing the bulk
535 water content, the condensation temperatures are significantly lowered, especially when the
536 water content is multiplied by a factor of 10. Again, this illustrates that our thermodynamic
537 calculations can be adapted to specific conditions in view of a more comprehensive modeling
538 of condensation in a nuclear cavity.
539 It should be emphasized here that the processes that take place right after the explosion (until
540 radioxenon release to the atmosphere) are the most significant in determining the relative
541 proportion of xenon isotopes (note that U and Pu have similar radioxenon fission yields), as
542 during atmospheric transport the xenon isotope abundances are only controlled by
543 radioactive decay.
544
545 **9. Implications of condensation on radioxenon**
546 As temperature and pressure are decreasing in the nuclear cavity, the condensation of In, Sn,
547 Sb, Te and I, the successive precursors to radioxenon, has a direct consequence on the final
548 accumulation of radioxenon, since the cooling rate can be fast relative to the escape rate of
549 xenon. For a quantitative estimate of these effects, one would need a precise knowledge of
550 the timescale leading to the fractionation of these precursors from the original gas phase. This

551 could be obtained by coupling the condensation calculations, the cooling history of the cavity
552 and its fractured chimney and the decay chains leading to radioxenon. As the thermo-chemical
553 evolution of nuclear cavities can be complex (see section 8.2), various scenarios should be
554 taken into account. Such an approach goes well beyond the scope of the present study and
555 will be the subject of future work.
556 In the meantime, our calculations can be used to illustrate the consequences of differential
557 condensation from a qualitative viewpoint. It is shown here that indium should rapidly be lost
558 by condensation upon cooling, due to its condensation temperature higher than 3000 K (Table
559 5). However, the half-lives of ^{131}In, ^{131m}In and ^{133}In are 0.28s, 0.35s and 163 ms, respectively,
560 which means that their lifetimes are too short relative to the cooling timescale in the 3000-
561 4000 K range (>30 s, Chapin 1970) to be affected by condensation. Had we used the boiling
562 temperature of pure In (2350 K) as in Carrigan et al. (2020), the conclusion would have been
563 identical since in this temperature range the cooling is even slower, which leaves no time for
564 condensation before radioactive decay.
565 The situation is different for the Sn isotopes ^{131}Sn, ^{133}Sn and ^{135}Sn, with half-lives of 56 s, 1.45
566 s and 520 ms, respectively. In this case, there could be an effect on ^{131}Sn with the consequence
567 that there would be a smaller in-growth of ^{131}Xe due to partial condensation before decay
568 (this effect could be enhanced by the large temperature interval for Sn condensation, e.g.
569 Figure 6). Similarly to In isotopes, ^{135}Sn would rapidly decay before condensation could take
570 place. The cases of Sb and Te are more difficult to assess qualitatively as the condensation
571 temperatures are lower and the half-lives of intermediate isotopes are longer. Thus,
572 deciphering the relative contribution of condensation and decay would require quantitative
573 modeling. For example, the half-life of ^{131}Te (25 min) combined with a condensation
574 temperature of 2040 K at 50 bars suggests that over that timescale both the temperature and
575 pressure in the cavity should have dropped significantly (e.g. Chapin 1970) to a level where
576 condensation of Te would compete with its decay.
577 Overall, our results suggest that a reliable estimate of the quantity of xenon available for
578 migration out of the nuclear cavity and the relative abundances of the radioactive xenon
579 isotopes used as signatures for underground nuclear testing should not ignore: (i)
580 condensation of the radioxenon precursors, (ii) determination of the true condensation
581 temperatures based on actual thermodynamic data, (iii) the deviation of the condensation
582 temperatures from boiling temperatures and from thermodynamic ideality, (iv) the

583 dependence of condensation temperatures on the host rock composition (and its water
584 content), (v) the dependence of condensation temperatures on pressure in rapidly evolving
585 environments such as underground explosions (vi) the role of vapor isolation, if that process
586 can be considered to have been effective.
587 In the longer term, by combining the thermodynamic properties of elements (as derived in
588 this study) with a physical model for the thermal evolution of the cavity (e.g. Chapin, 1970),
589 as well as a reactive transport model for the vapor above the nuclear cavity (Sun and Carrigan,
590 2016; Pazdniakou et al., 2022), one should be able to obtain a more realistic picture of the
591 processes happening after the explosion. This type of information should provide better
592 estimates of the radionuclide source term potentially emitted to the atmosphere, thereby
593 providing a better diagnostic tool than previous more simplistic models.
594

595 **10. Conclusions**

596 This study highlights that thermodynamic modeling is essential for a proper evaluation of the
597 effect of condensation of In, Sn, Sb, Te and I in a nuclear cavity following an underground
598 nuclear explosion. A model that properly predicts the behavior of these elements must include
599 realistic values of their activity coefficients in silicate melts of given compositions and take
600 into account the variation of these parameters over a large range of temperatures and
601 pressures. If these parameters are not accounted for, there can be large deviations by several
602 hundreds of kelvins in the condensation temperature of the elements considered here.
603 Furthermore, condensations of some radionuclides are shown to occur over a temperature
604 range as large as 2000 K, in strong contrast with the often referred to Heaviside function.
605 These determinations of condensation temperatures and vapor pressure evolutions can also
606 take into account potential complications arising in the conditions of underground nuclear
607 explosions, such as to the effect of vapor isolation from the magma, or addition of extra water
608 from devolatilization of the country rock, or even the kinetic barriers to condensation.
609 Since the radionuclides considered here are the precursors of radioxenon (^{131m}Xe, ^{133}Xe,
610 ^{133m}Xe, ^{135}Xe) used in the detection and discrimination of underground nuclear testing, an
611 incorrect estimate in the condensation behavior of these elements could lead to slanted
612 estimates of the source term used in atmospheric transport modeling to interpret data from
613 the CTBT international monitoring system. The reader is referred to Ringbom et al. (2014) for
614 a worked example of the interpretation of such data.

In addition, as condensation varies with temperature, pressure and the bulk chemical composition of the system, a heterogeneous spatial distribution of the condensed radionuclides is expected in the nuclear cavity, notably among the variety of the melts produced over time (e.g., Boardman et al., 1964, Schwartz et al., 1984). This could have a strong impact on the nature and quantity of the radionuclides available for migration, particularly when estimating the hydrologic source term (e.g., Tompson et al., 2011).

Thanks to our determinations of condensation temperatures and vapor pressure in relevant conditions, it should be possible to give better estimates of the fluxes of the precursor isotopes to radioactive xenon potentially emitted from nuclear explosions as a function of the pressure and temperature of the system. As mentioned above, the dynamics of cavity formation and evolution may complicate the simple picture of a closed system condensation. Nevertheless, our work provides more realistic parameters that can be used to extend earlier studies based on pure substances, allowing better modeling of these complex systems.

Acknowledgements:

We thank two anonymous reviewers for their valuable comments that greatly helped improve the manuscript. This study was partly funded by the ERC project COSMOKEMS # 694819.

Figure captions

Figure 1 Radioactive decay chains for the 131, 133, and 135 isobars leading to xenon. Horizontal arrows denote isomeric transitions, with the superscript m for the metastable nuclide; other arrows denote β^- decay. Numbers on arrows indicate the half-lives with the following units: second (s), minute (min), hours (hr) days (d), millions of year (Myr). Data are taken from the joint evaluated fission and fusion nuclear data library 3.3 (Plompen et al., 2020). Cadmium (Cd) is neglected in this condensation study owing to its very short half-life, as well as the daughter products of xenon (Cs and Ba) as their trapping in the magma has no effect on the Xe inventory.

Figure 2 Calculated activity coefficient of SnO_2 in a silicate melt based on metal-silicate partition coefficient from Righter et al. (2017).

Figure 3 Condensation curves for a basaltic composition at 50 bar, volatility controlled by the pure substances, TeO_2, SnO_2, In_2O_3, SbO_2, $Ca(IO_3)_2$. The fraction in the vapor is calculated using the ratio of the molar abundance in the vapor to the initial molar abundance in the bulk system.

Figure 4 Condensation curve for a basaltic composition at 50 bar assuming an ideal mixture between In_2O_3, SnO_2, SbO_2, TeO_2 and $Ca(IO_3)_2$ and the silicate melt ($\gamma_{MxOy} = 1$).

Figure 5 Condensation curves of I, Te, Sb, Sn, and In for a granodiorite composition at (a) 1 bar, (b) 10 bar, (c) 50 bar and (d) 100 bar, as labeled on the diagrams.

Figure 6 Condensation curves of I, Te, Sb, Sn, and In for a basalt composition at (a) 1 bar, (b) 10 bar, (c) 50 bar and (d) 100 bar, as labeled on the diagrams.

Figure 7 (a) Variations of the condensation temperature (K) as a function of pressure (bars) for a granodiorite composition. (b) Variations of the condensation temperatures (K) as a function of pressure (bars) for a basalt composition.

Figure 8 (a) Diffusion length scales of Te and Sb in a basaltic melt as a function of temperature. Diffusion coefficient data from MacKenzie and Canil 2008. (b) condensation temperatures for In, Sn, Sn and Te in the case where vapor is isolated from the magma at 50 bars and 3500 K. The curves with a dashed line (identical color code) represent the condensation for the case with no vapor isolation (similar to Figure 6 at 50 bar).

Figure 9 Condensation temperatures calculated for In, Sn, Sb and Te at 10 bars for the basaltic composition with a water content increased by a factor of 2 (short dash line) and a factor of 10 (long dash line) compared to the original one (solid line) as given in Table 2.

References:

Achim, P., Generoso, S., Morin, M., Gross, P., Le Petit, G. and Moulin, C. (2016) Characterization of Xe-133 global atmospheric background: Implications for the International Monitoring System of the Comprehensive Nuclear-Test-Ban Treaty. J. Geophys. Res.: Atmospheres 121, 4951-4966. https://doi.org/10.1002/2016JD024872

Barin, I. (1995) Thermochemical Data of Pure Substances, 2nd Edition, VCH Publishers, Inc., New York, NY (USA), 2003 pp.

Boardman, C.R., Rabb, D.D., McArthur, R.D., 1964. Responses of four rock mediums to contained nuclear explosions. Journal of Geophysical Research 69, 3457-3469. https://doi.org/10.1029/JZ069i016p03457

Borg, I.Y., 1975. Radioactivity Trapped in Melt Produced by a Nuclear Explosion. Nuclear Technology 26, 88-100. https://doi.org/10.13182/NT75-A24406

Brode, H.L. (1964) A Review of nuclear explosion phenomena pertinent to protective construction, United States Air force project Rand, Rand corp. R-425-PR, 65 p. https://apps.dtic.mil/sti/pdfs/AD0601139.pdf, last accessed 10/12/2022.

Butkovich, T.R., 1974. Rock melt from an underground nuclear explosion, Lawrence Livermore Laboratory, report UCRL-51554, 14 pp. https://www.osti.gov/servlets/purl/4321502

Butkovich, T.R., 1974. Some studies of deeply buried high explosive rock fracturing, Lawrence Livermore Laboratory report UCID-16526, 23 pp.

Carrigan, C., Sun, Y., Hunter, S.L. Ruddle, D.G., Wagoner J. L., Myers K. B. L., Emer D.F., Drellack S.L. & Chipman V.D. (2016) Delayed signatures of underground nuclear explosions. Sci Rep 6, 23032. https://doi.org/10.1038/srep23032

Carrigan, C.R., Sun, Y., Pili, E., Neuville, D.R. and Antoun, T. (2020) Cavity-melt partitioning of refractory radionuclides and implications for detecting underground nuclear explosions. J. Environ. Radioact. 219, 106269. https://doi.org/10.1016/j.jenvrad.2020.106269

Castagnola, D.C., Carnahan, C.L. (1971) Prediction of cavity radius and estimation of cavity gas temperatures produced by a contained underground nuclear explosion, U. S Atomic Energy Commission, 45 pp. https://inis.iaea.org/collection/NCLCollectionStore/_Public/04/051/4051243.pdf, last accessed 10/12/2022

Cicconi, M.R., Pili, E., Grousset, L., Florian, P., Bouillard, J.C., Vantelon, D., Neuville, D.R. (2019) Iodine solubility and speciation in glasses, Sci. Rep. 9 (1), 1-13.

Cicconi, M.R., Pili, E., Grousset, L., Neuville, D.R. (2019) The influence of glass composition on iodine solubility, MRS Advances 4 (17-18), 971-979. https://doi.org/10.1038/s41598-019-44274-4

728 Chapin, C.E., (1970) Cavity pressure history of contained nuclear explosions, Proceedings. Vol.
729 1, Symposium on engineering with nuclear explosives; Las Vegas, NV (United States), p. 463-
730 480. https://inis.iaea.org/collection/NCLCollectionStore/_Public/36/010/36010774.pdf
731
732 Coblentz, D. and Pabian, F. (2015) Revised Geologic Site Characterization of the North Korean
733 Test Site at Punggye-ri. Sci. Glob. Secur. 23, 101-120.
734 https://scienceandglobalsecurity.org/archive/sgs23coblentz.pdf , last accessed 10/12/2022.
735
736 Costa, G.C.C., Jacobson, N.S., Fegley Jr, B. (2017) Vaporization and thermodynamics of
737 forsterite-rich olivine and some implications for silicate atmospheres of hot rocky exoplanets,
738 Icarus 289, 42-55. https://doi.org/10.1016/j.icarus.2017.02.006
739
740 Dupuy, C., Vidal, P., Maury, R., Guille, G. (1993) Basalts from Mururoa, Fangataufa and
741 Gambier islands (French Polynesia): Geochemical dependence on the age of the lithosphere.
742 Earth Planet. Sci. Lett., 117(1): 89-100. https://doi.org/10.1016/0012-821X(93)90119-T
743
744 Egorov, V.A., Kolobashkin, V.M., Kudryashov, N.A., (1979) Gas temperature and pressure in
745 the cavity of an underground explosion. Combust Explos Shock Waves, 15(5): 654-659.
746 https://doi.org/10.1007/BF00740597
747
748 Gortais, J., Hodaj, F., Allibert, M., Welter, J.-M. (1994) Equilibrium Distribution of Fe, Ni, Sb,
749 and Sn between Liquid Cu and a CaO-Rich Slag, Metall. Materials Trans. B, 25B, 645-651.
750 https://doi.org/10.1007/BF02655172
751
752 Higgins, G.H., (1970) Underground nuclear explosions, Proceedings. Vol. 1, Symposium on
753 engineering with nuclear explosives; Las Vegas, NV (United States), p. 29-42.
754 https://inis.iaea.org/collection/NCLCollectionStore/_Public/36/010/36010774.pdf
755
756 Higgins, G.H., Butkovich, T.R. (1967) Effect of water content, yield, medium and depth of burst
757 on cavity radii. Lawrence Radiation Laboratory report UCRL-50203, 28 pp.
758

759 Hirth, J. P., Pound, G. M. (1963) Progress in Materials Science: Nucleation and Growth Kinetics.
760 Condensation and Evaporation. Ed B. Chalmers, Macmillan 192 pp.
761
762 Hourdin, F. Issartel, J.-P. (2000) Sub-surface nuclear tests monitoring through the CTBT Xenon
763 Network, Geophys. Res. Lett., 27, 2245-2248. https://doi.org/10.1029/1999GL010909
764
765 IAEA (1998a) Radiological Conditions at the Semipalatinsk Test Site, Kazakhstan.
766 STI/PUB/1063. International Atomic Energy Agency, Vienna, 51 p.
767 https://www.iaea.org/publications/4741/radiological-conditions-at-the-semipalatinsk-test-
768 site-kazakhstan , last accessed 10/12/2022
769
770 IAEA (1998b). The Radiological Situation at the Atolls of Mururoa and Fangataufa. Main report.
771 STI/PUB/1028. International Atomic Energy Agency, Vienna, 310 p.
772 https://www.iaea.org/publications/4728/the-radiological-situation-at-the-atolls-of-
773 mururoa-and-fangataufa, last accessed 12/10/2022
774
775 Johnston, M.D., Jahanshahi, S., Zhang, L., Lincoln, F.J. (2010) Effect of Slag Basicity on Phase
776 Equilibria and Selenium and Tellurium Distribution in Magnesia-Saturated Calcium Iron Silicate
777 Slags, Metall. Materials Trans. B 41B, 625-635. Doi: 10.1007/s11663-010-9355-7
778
779 Jolivet, V., Morizet, Y., Paris, M., Suzuki-Muresan, T. (2020) High pressure experimental study
780 on iodine solution mechanisms in nuclear waste glasses. J. Nucl. Mater. 152112.
781 https://doi.org/10.1016/j.jnucmat.2020.152112
782
783 Lee, W. H., and Gard, L. M. Jr. (1971) Summary of the subsurface geology of the Cannikin Site,
784 Amchitka Island, Alaska: Reston, VA, U.S. Geological Survey, 24 p.
785
786 Lide, D.R. (1990) CRC Handbook of Chemistry and Physics, 70th ed. CRC Press, Boca Raton, FL,
787 p. 2388.
788
789 Lodders, K., (2003) Solar System Abundances and Condensation Temperatures of the
790 Elements. Astrophys. J. 591(2): 1220-1247. https://doi.org/10.1086/375492

Ma, Z. (2001) Thermodynamic description for concentrated metallic solutions using interaction parameters. Metall. Mater. Trans. B 32, 87–103. https://doi.org/10.1007/s11663-001-0011-0

MacKenzie, J.M. Canil, D. (2008) Volatile heavy metal mobility in silicate liquids: Implications for volcanic degassing and eruption prediction, Earth and Planetary Science Letters, 269, 488-496. https://doi.org/10.1016/j.epsl.2008.03.005.

McKeown, D.A., Muller, I.S., Pegg, I.L. (2015) Iodine valence and local environments in borosilicate waste glasses using X-ray absorption spectroscopy. J. Nucl. Mater. 456, 182-191. https://doi.org/10.1016/j.jnucmat.2014.09.033

Mendoza, D.G., Hino, M., Itagaki, K. (2001) Volatility and vapor pressure measurements of antimony and arsenic components in $CaO\text{-}SiO_2\text{-}FeO_{1.5}$ slags at 1,573 K by transpiration method. J. Min. Mater. Process., 117, 901-906. https://doi.org/10.2473/shigentosozai.117.901

Musselwhite, D.S. (1995) Experimental geochemistry of iodine, argon and xenon: Implications for the outgassing histories of the Earth and Mars, PhD Thesis University of Arizona, 151 pp. https://citeseerx.ist.psu.edu/viewdoc/download?doi=10.1.1.956.520&rep=rep1&type=pdf, last accessed 10/12/2022

Musselwhite, D.S., and Drake, M.J. (2000) Early Outgassing of Mars: Implications from Experimentally Determined Solubility of Iodine in Silicate Magmas. Icarus 148, 160–175. https://doi.org/10.1006/icar.2000.6427

Mutaftschiev, B. (2001)The atomistic nature of crystal growth, Berlin, Springer, 368 pp. https://doi.org/10.1007/978-3-662-04591-6

Nagamori, M., Mackey, P.J. (1978) Thermodynamics of Copper Matte Converting: Part II. Distribution of Au, Ag, Pb, Zn, Ni, Se, Te, Bi, Sb and As Between Copper, Matte and Slag in the Noranda Process, Metall. Trans. B, 9B, 567-579. https://doi.org/10.1007/BF03257205

Norris, C.A. (2016) Volatilities of Trace Elements in Silicate Melts, PhD Thesis Oxford University, 319 pp. https://www.academia.edu/49164048/Volatilities_of_Trace_Elements_in_Silicate_Melts, last accessed 10/12/2022.

O'Neill, H.St.C., Eggins, S.M. (2002) The effect of melt composition on trace element partitioning: an experimental investigation of the activity coefficients of FeO, NiO, CoO, MoO_2 and MoO_3 in silicate melts, Chem. Geol. 186, 151– 181. https://doi.org/10.1016/S0009-2541(01)00414-4

Olsen, C.W. (1967) Time History of the Cavity Pressure and Temperature Following a Nuclear Detonation in Alluvium, J. Geophys. Res. 72, 5037-5041. https://doi.org/10.1029/JZ072i020p05037

Pazdniakou, A., Mourzenko, V., Thovert, J.-F., Adler, P.M., Pili, E. (2022). Two-phase flow, heat and mass transfer and tracer transport to the atmosphere from underground nuclear cavities through fractured porous media. Pure Appl. Geophys. https://doi.org/10.1007/s00024-022-03038-4

Pelton, A.D. (1999) Thermodynamic Calculation of Gas Solubilities in Oxide Melts and Glasses, Glastechnische Berichte, 72, 214-226.

Plompen, A.J.M. et al. (2020) The joint evaluated fission and fusion nuclear data library, JEFF-3.3. Eur. Phys. J. A 56, 181. https://doi.org/10.1140/epja/s10050-020-00141-9

Rankin, W.J. (1986) The Slag-Metal Equilibrium in Tin Smelting, Metall. Trans. B 17B, 61-68. https://doi.org/10.1007/BF02670819

Ringbom, A., Axelsson, A., Aldener, M., Auer, M., Bowyer, T.W., Fritioff, T., Hoffman, I., Khrustalev, K., Nikkinen, M., Popov, V., Popov, Y., Ungar, K. and Wotawa, G. (2014) Radioxenon detections in the CTBT international monitoring system likely related to the announced nuclear test in North Korea on February 12, 2013. J. Environ. Radioact. 128, 47-63. DOI: 10.1016/j.jenvrad.2013.10.027

Righter, K., Nickodem, K., Pando, K., Danielson, L., Boujibar, A., Righter, M., Lapen, T.J. (2017) Distribution of Sb, As, Ge, and In between metal and silicate during accretion and core formation in the Earth, Geochim. Cosmochim. Acta 198, 1–16. https://doi.org/10.1016/j.gca.2016.10.045

Riley, B. J., Schweiger, M. J., Kim, D.S., Lukens, W.W., Williams, B.D., Iovin, C., Rodriguez, C.P., Overman, N.R., Bowden, M.E., Dixon, D.R., Crum, J.V., McCloy, J.S., Kruger, A.A. (2014) Iodine solubility in a low-activity waste borosilicate glass at 1000°C. J. Nucl. Mater. 452, 178-188. https://doi.org/10.1016/j.jnucmat.2014.04.027

Schwartz, L., Piwinskii, A., Ryerson, F., Tewes, H. and Beiriger, W. (1984) Glass produced by underground nuclear-explosions. J. Non Cryst. Solids 67, 559-591. https://doi.org/10.1016/0022-3093(84)90176-5

Shuva, M.A.H., Rhamdhani, M.A., Brooks, G.A., Masood, S. Reuter, M.A. (2016) Thermodynamics data of valuable elements relevant to e-waste processing through primary and secondary copper production: a review, J. Clean. Prod. 131 (2016) 795-809. https://doi.org/10.1016/j.jclepro.2016.04.061

Sinnock, S. (1982) Geology of the Nevada Test Site and Nearby Areas, Southern Nevada, Sandia Report, SAND82-2207, 58 pp. https://www.nrc.gov/docs/ML0330/ML033020461.pdf, last accessed 10/12/2022.

Smith, D.K. (1995) Characterization of nuclear explosive melt debris. Radiochimica Acta 69, 157-167.. https://doi.org/10.1524/ract.1995.69.3.157

885 Smith, D.K., Finnegan, D.L., Bowen, S.M. (2003) An inventory of long-lived radionuclides
886 residual from underground nuclear testing at the Nevada test site, 1951-1992. Journal of
887 Environmental Radioactivity 67, 35-51. DOI:10.1016/S0265-931X(02)00146-7
888
889 Smith, D.K., Nagle, R.J., Kenneally, J.M. (1996) Transport of gaseous fission products adjacent
890 to an underground nuclear test cavity. Radiochimica Acta 73, 177-183.
891 https://doi.org/10.1524/ract.1996.73.4.177
892
893 Sun, Y. and Carrigan, C.R. (2016) Thermally driven advection for radioxenon transport from an
894 underground nuclear explosion. Geophys. Res. Lett. 43, 4418-4425.
895 https://doi.org/10.1002/2016GL068290
896
897 Sun, Y., Carrigan, C., Cassata, W., Hao, Y., Ezzedine, S. and Antoun, T. (2021) A closed-form
898 solution for source-term emission of xenon isotopes from underground nuclear explosions.
899 Transp. Porous Med. 139, 131–153. https://doi.org/10.1007/s11242-021-01650-x
900
901 Sun, Y., Carrigan, C. and Hao, Y. (2015) Radioxenon production and transport from an
902 underground nuclear detonation to ground surface. Pure Appl. Geophys. 172, 243–265.
903 https://doi.org/10.1007/s00024-014-0863-2
904
905 Sun, Y., Carrigan, C.R., Pili, E. and Antoun, T. (2022) Implications of Underground Nuclear
906 Explosion Cavity Evolution for Radioxenon Isotopic Composition. Pure Appl. Geophys.
907 https://doi.org/10.1007/s00024-022-03026-8
908
909 Tan P., Neuschutz, D. (2001) A Thermodynamic Model of Nickel Smelting and Direct High-
910 Grade Nickel Matte Smelting Processes: Part I. Model Development and Validation, Metall
911 Mater. Trans. B 32, 341–351. https://doi.org/10.1007/s11663-001-0057-z
912
913 Taylor, R.W. (1973) Thermal Effects of Underground Nuclear Explosions. Nucl. Tech. 18(2):
914 185-193. https://doi.org/10.13182/NT73-A31287
915

The Japan Society for the Promotion of Science and The Nineteenth Committee on Steelmaking (1988) Part 2: Recommended values of activity and activity coefficients, and interaction parameters of elements in iron alloys. In Steelmaking Data Sourcebook. Gordon and Breach Science Publishers, New York. pp. 273–297.

Tompson, A.F.B., Zavarin, M., McNab, W.W., Carle, S.F., Shumaker, D.E., Lu, C., Sun, Y., Pawloski, G.A., Hu, Q. and Roberts, S.K. (2011) Hydrologic Source Term Processes and Models for Underground Nuclear Tests at Rainier Mesa and Shoshone Mountain, Nevada National Security Site (Rev. 1.0), report LLNL-TR-483852. https://www.osti.gov/biblio/1544496, last accessed 10/12/2022.

UNODA, (1995) International Monitoring System Expert Group Report based on Technical Discussions held from 6 February to 3 March 1995. Conference on Disarmament, United Nations Office for Disarmament Affairs, document CD/NTB/WP.224. 97 pp.

Wood, B.J., Wade, J., (2013) Activities and volatilities of trace components in silicate melts: a novel use of metal-silicate partitioning data. Contrib. Min. Pet. 166, 911-921. https://doi.org/10.1007/s00410-013-0896-z

Wood, B.J., Smythe, D.J., Harrison, T. (2019) The condensation temperatures of the elements: A reappraisal. Am. Min. 104, 844-856. https://doi.org/10.2138/am-2019-6852CCBY

938 Figure 1

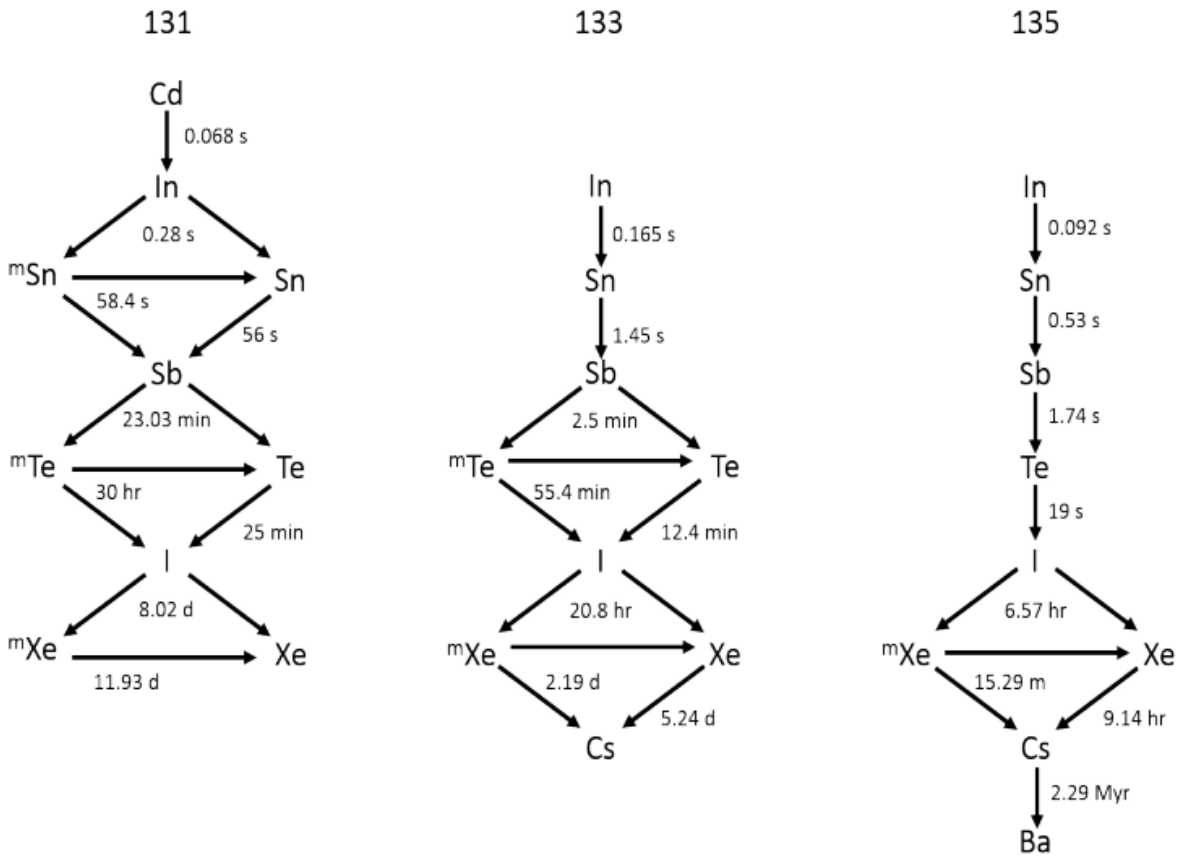

939

940

941 Figure 2

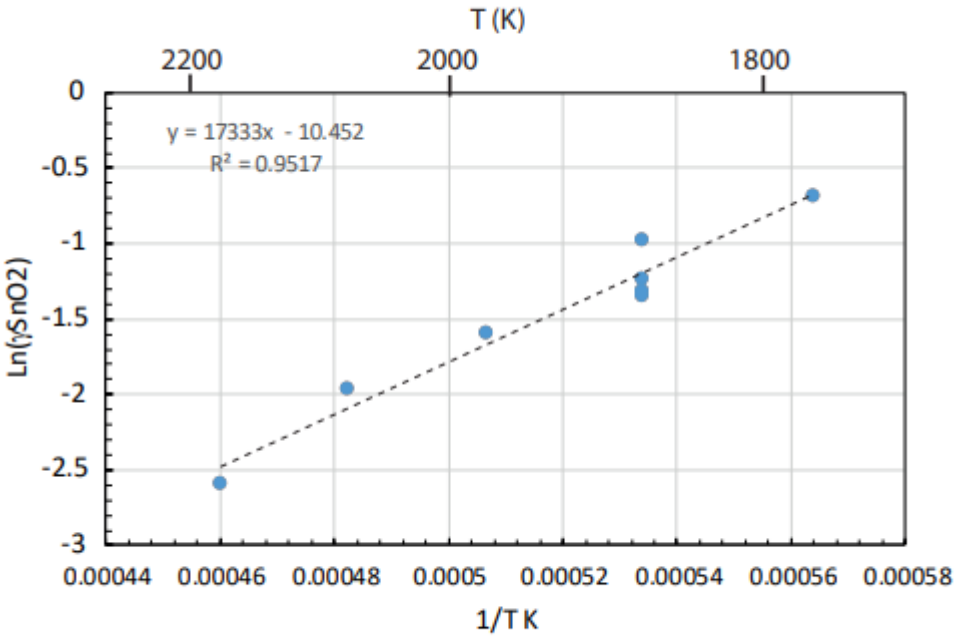

942

943

944 Figure 3

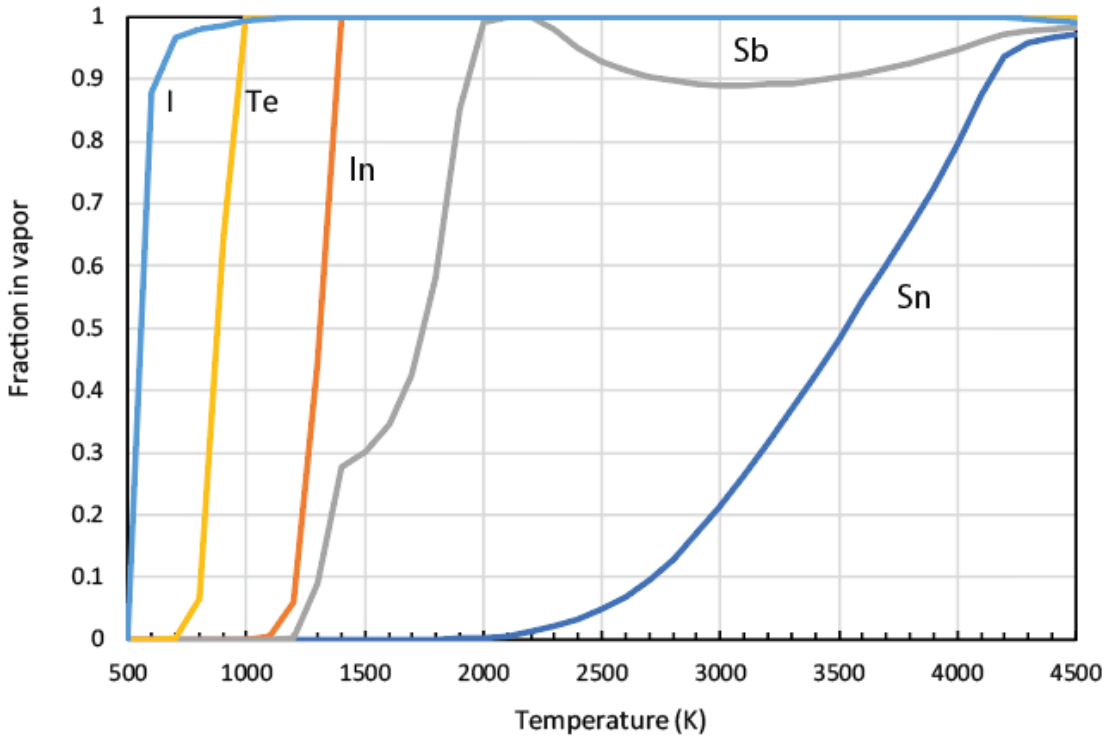

945

946

947 Figure 4

948

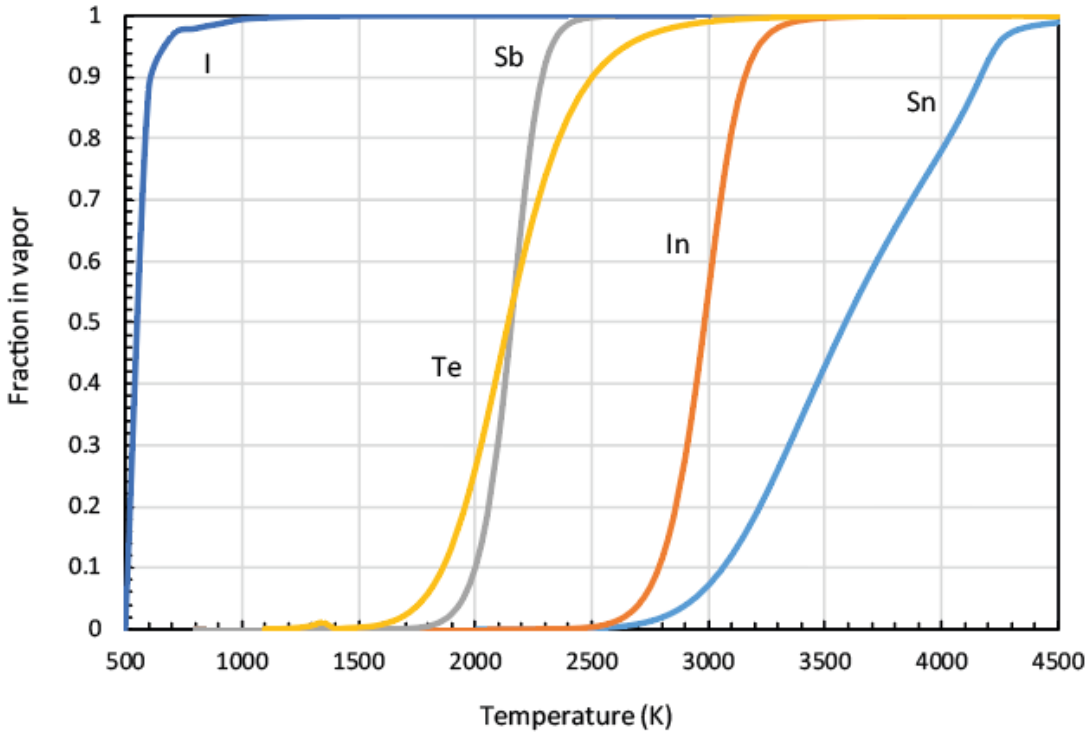

949

950

951 Figure 5

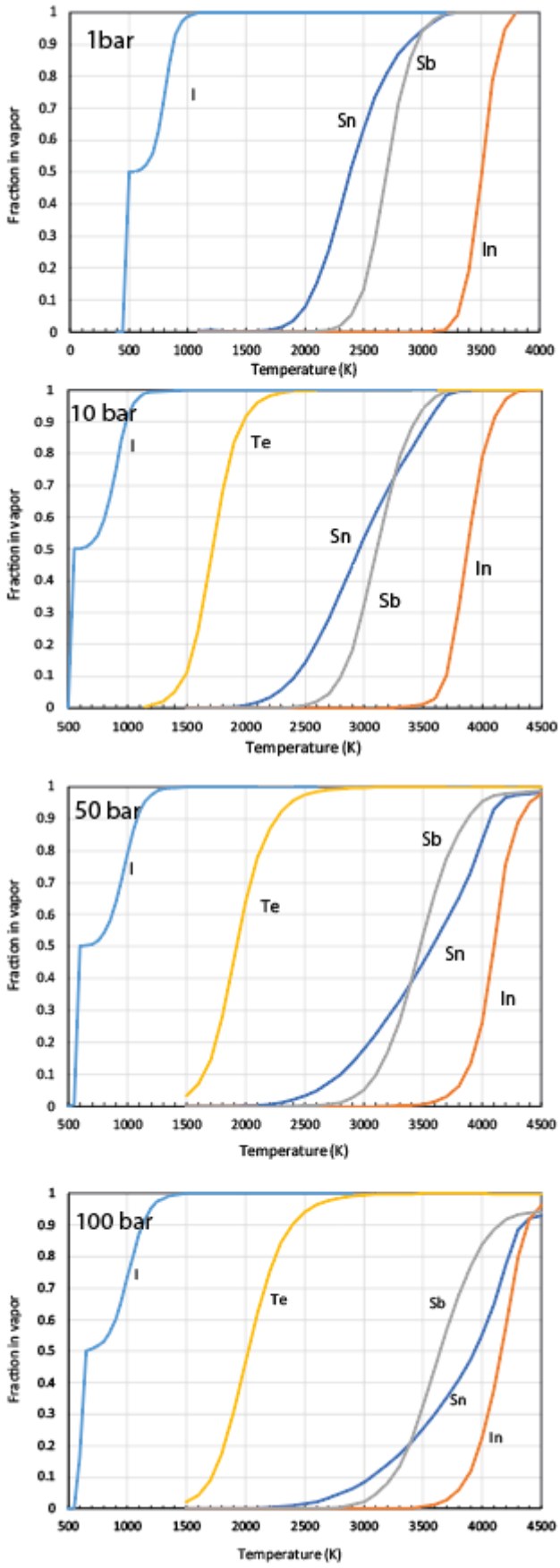

952

953 Figure 6

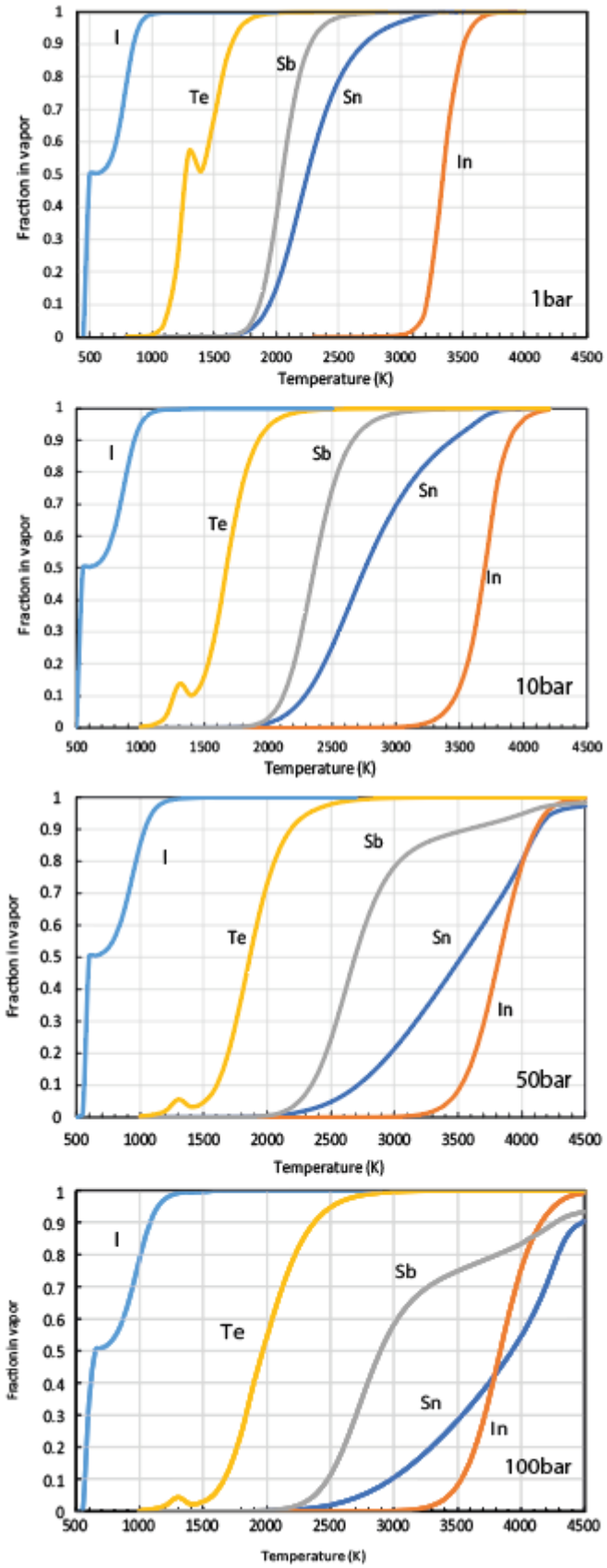

954

955

956 Figure 7

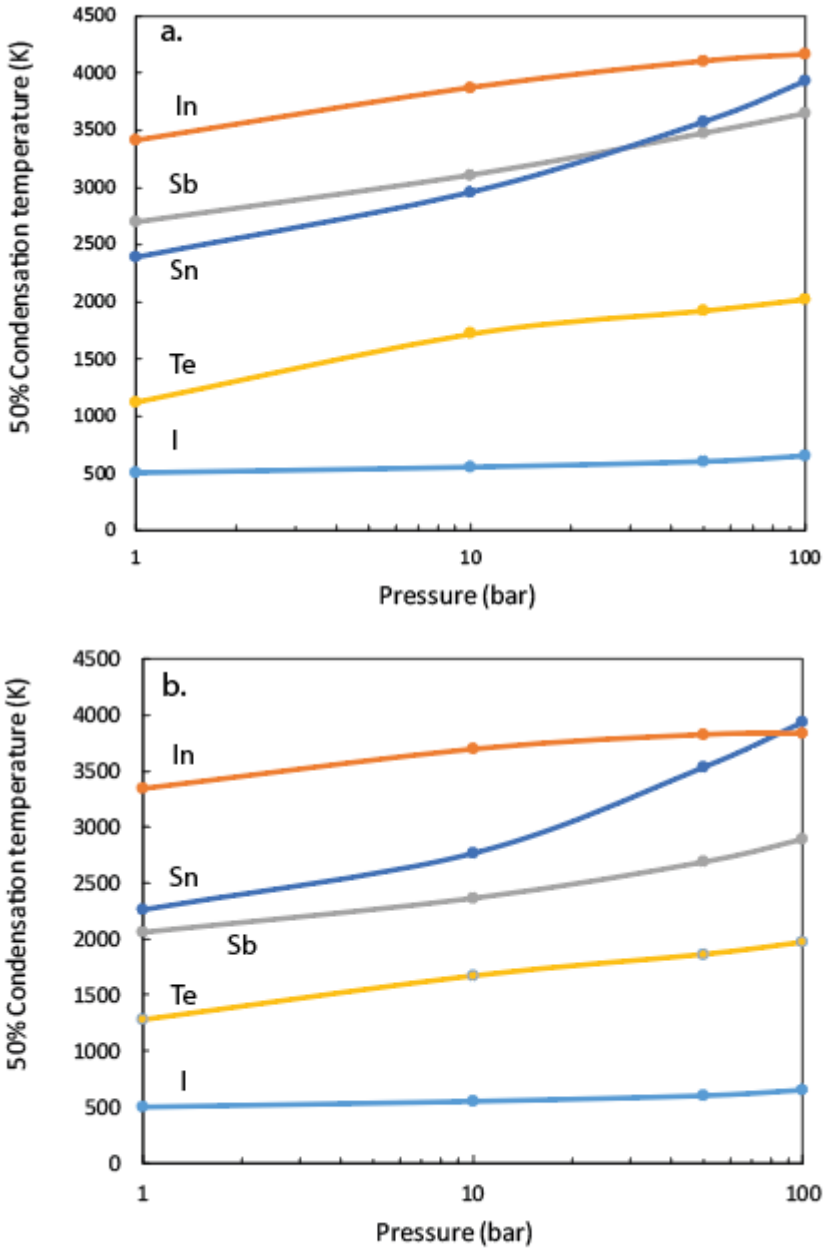

957

958

959 Figure 8

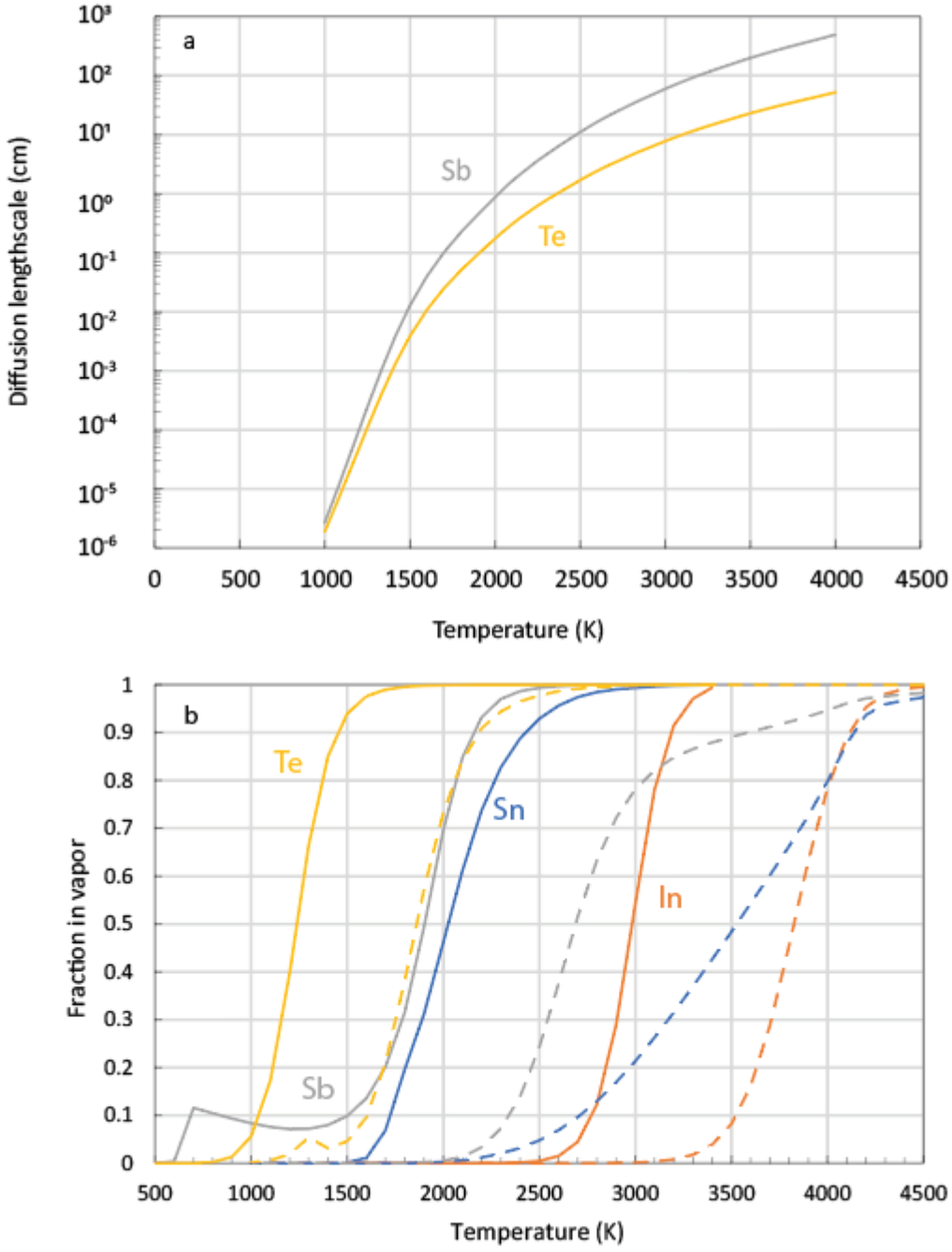

960

961

962 Figure 9

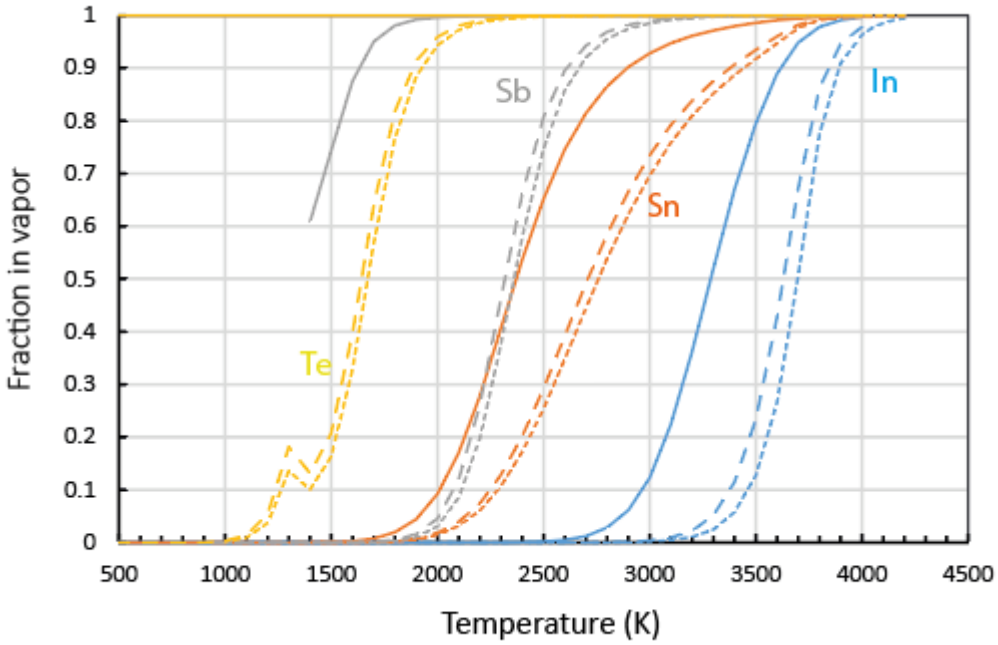

963